J Mater Sci: Mater Med (2013) 24:2873–2880
DOI 10.1007/s10856-013-5024-0

Synthesis and characterization of calcium phosphate loaded with Ho-166 and Sm-153: a novel biomaterial for treatment of spine metastases

B. A. Donanzam · T. P. R. Campos · I. Dalmázio · E. S. Valente

Received: 27 March 2013 / Accepted: 26 July 2013 / Published online: 3 August 2013

Abstract Spine metastases are a common and painful complication of cancer. A novel concept of treatment combines the in situ vertebroplasty with radiotherapy employing radioactive bone cement into the human vertebrae. Thus, investigations concerning possible bioactive and radioactive cements become a relevant theme. In this work, we have synthesized calcium phosphate bioceramics incorporated with Ho and Sm nuclides using sol–gel technique. Characterizations were performed using X-ray diffractometry, infrared spectroscopy, scanning electron microscopy, instrumental neutron activation analysis, and gamma spectroscopy. Results showed bioceramics composed by multiphasic calcium phosphates along with holmium and samarium phosphates, with 8.9 and 13.7 % of Sm and Ho in weight, respectively. After neutron activation, the Ho-166 and Sm-153 beta-emitters were identified and quantified on the bioceramics with activities estimated at 32.5 and 14.5 MBq/mg of Sm-153 and Ho-166 bioceramic powder, respectively. These radioactive calcium phosphate bioceramics can compose suitable radioactive cements to radiovertebroplasty.

B. A. Donanzam · T. P. R. Campos
Departamento de Engenharia Nuclear, Universidade do Federal de Minas Gerais (UFMG), Avenida Presidente Antônio Carlos, 6627, Belo Horizonte, MG 31270-901, Brazil

I. Dalmázio (✉)
Serviço do Reator e Técnicas Analíticas, Centro de Desenvolvimento da Tecnologia Nuclear (CDTN), Avenida Presidente Antônio Carlos, 6627, Belo Horizonte, MG 31270-901, Brazil
e-mail: id@cdtn.br

E. S. Valente
Unidade de Pesquisa e Produção de Radiofármacos, Centro de Desenvolvimento da Tecnologia Nuclear (CDTN), Avenida Presidente Antônio Carlos, 6627, Belo Horizonte, MG 31270-901, Brazil

1 Introduction

Spinal metastases are a common manifestation of many types of cancer. Specifically, metastatic lesions in the spine were present in 90, 74 and 45 % of patients who died from prostate, breast and lung cancer, respectively [1]. Vertebral metastases cause pain and due to the proximity of the spinal cord can lead to serious neurological complications resulting from vertebral collapse. Treatment must address the tumor itself as well as the bone structural fragility [2]. The conventional treatment often occurs in two steps, a surgical procedure in which polymethylmethacrylate (PMMA) bone cement is injected into the vertebral body to restore bone strength (vertebroplasty), followed by multiple daily radiotherapy sessions to control tumor growth [3].

The most common type of radiotherapy for spinal metastases is the external beam radiation therapy (EBRT). Although EBRT delivers radiation to the vertebral body effectively, adjacent radiosensitive tissues such as the spinal cord are also irradiated [4, 5]. A safe treatment must provide a maximum dose to the tumor limiting the spinal cord dose. In order to achieve tumor control dose minimizing collateral damage to normal tissue, EBRT is applied on daily fractions for ten sessions. Intensity modulated radiation therapy (IMRT) and stereotactic body radiation therapy (SBRT) have emerged as modern radiotherapy techniques, however both techniques still irradiate the spinal cord (albeit to a lesser extent) and are of high cost [6, 7].

Recently, a new therapy modality, named radiovertebroplasty, proposed to combine the vertebroplasty to radiotherapy employing radioactive bone cement, i.e. bone cement

incorporating radioactive radionuclides [8, 9]. If effective, this approach shall integrate radiation therapy and the surgical strength-restoration procedure into a single treatment procedure. In addition, after the implant of radioactive bone cement into the tumor, beta-emitter radionuclides provide radioactive emissions that penetrate few millimeters toward the adjacent bone/tumor interface, potentially imparting higher dose to the target bone with minimal dose to the spinal cord and other normal tissue nearby. Computational dosimetric analysis showed the properties of some radioisotopes on the radiovertebroplasty simulation [3, 8–11]. Preliminaries clinical investigations of injecting PMMA mixed with Sm-153-EDTMP (ethylenediamine tetramethylene phosphonate) have revealed a procedure feasible and safe with good pain control, but longer follow-up is needed to evaluate the toxicity and tumor control [12–14]. Up to now, there are few studies comprising the synthesis of radioactive biomaterials focused on this purpose.

Polymethylmethacrylate is often employed as bone cement. It has good mechanical performance and it is inerted to the human body [15]. At the same time, biomaterials based on calcium phosphates ceramics (CaPs) have been extensively investigated as bone substitutes due to their similar chemical characteristics and bioactive properties [16–20]. There are many kinds of calcium phosphates bioceramics, e.g., hydroxyapatite, tricalcium phosphate, octacalcium phosphate, dicalcium phosphate; each one provides distinct strength, stability and solubility in physiological environment. They have been explored in bone replacements, coatings on implants and bone cements in association with PMMA. Notably, the use of biphasic calcium phosphates hydroxyapatite/β-tricalcium phosphate has attracted much attention, owing to the possibility to control the bioresorbability [21, 22].

Taking account some suitable features, we suggest the composite PMMA/CaP-beta emitter as promising radioactive bone cement. In this study, the main goal is to investigate the synthesis and characterization of calcium phosphates incorporated with Ho and Sm (CaP–Ho and CaP–Sm). The elements Ho and Sm are precursors of the beta-emitters Ho-166 (half-life 1.12 days) and Sm-153 (half-life 1.93 days), respectively. These radioactive bioceramics when added on PMMA give rise to radioactive bone cement. The material composition held radioactive nuclides in enough concentration that supports its putative therapeutic use in radiovertebroplasty.

2 Materials and methods

2.1 Synthesis

Sol–gel route was the choice as synthesis technique for its simplicity, flexibility and low cost. Three types of bioceramics were prepared: calcium phosphate incorporated with holmium (CaP–Ho), calcium phosphate incorporated with samarium (CaP–Sm) and pure calcium phosphate (CaP) for comparison. The starting materials used in this synthesis were analytical grade reagents $Ca(NO_3)_2{\cdot}4H_2O$ (Labsynth, BRA) as the calcium source, H_3PO_4 (85 % solution, Reagen, BRA) as the phosphorus source, $Sm(NO_3)_3{\cdot}6H_2O$ (Aldrich, USA) as the samarium source, and Ho_2O_3 (Alfa Aesar, USA) as the holmium source. Previously, both calcium and samarium nitrates were dissolved in distilled water, and the holmium oxide was first dissolved in concentrated nitric acid and after diluted in distilled water. The molar ratios used in the synthesis were: 10(Ca):6(P) for CaP, 9(Ca):6(P):1(Ho) for CaP–Ho and 9(Ca):6(P):1(Sm) for CaP–Sm. The solutions were taken after stirring the reagents for 10 min. Aging was performed for 24 h at ambient temperature in a ceramic crucible. The solvents were eliminated by drying at 100 °C and then calcined in air at 700 °C. The resultant materials were powdered with mortar and pestle.

2.2 Characterization

2.2.1 X-Ray diffractometry (XRD)

Powder X-ray diffraction patterns were recorded with CuKα radiation on a diffractometer (Rigaku, model D/MAX Ultima automatic). The crystalline phases were qualitatively determined based on a comparison of the registered patterns with the ICDD powder diffraction file (PDF).

2.2.2 Fourier transform infrared spectroscopy (FTIR)

The infrared spectra were obtained on a Fourier-transform infrared spectrometer (Thermo Scientific, model Nicolet 380) with a resolution of 4 cm^{-1}, recorded in the range of 400–4000 cm^{-1}, using KBr pellets. The characteristic infrared absorption frequencies were analyzed to identify the chemical compositions.

2.2.3 Scanning electron microscopy (SEM)

Morphological characterizations were obtained by a scanning electron microscope (FEI, model Quanta 200 FEG) that was operated at accelerating voltage of 30 kV.

2.2.4 Instrumental neutron activation analysis (INAA)

Neutron activation of the samples was performed in TRIGA MARK I IPR-R1 research reactor. The elemental concentration of the powders was determined using the technique k_0-instrumental neutron activation analysis

(k_0-INAA), established at Laboratory of Neutron Activation Analysis in CDTN/CNEN [23].

2.2.5 Gamma spectroscopy

The gamma spectra were taken after the sample activation and registered the most abundant radioactive nuclides. They were recorded by a high-purity germanium detector Camberra, model GC5019, coupled to the multichannel analyzer (Camberra, model DSA 1000) with counting time of 500 s.

2.2.6 Theoretical estimation of specific activity

The theoretical estimations of the induced activities of each radionuclide were carried out. Each possible radionuclide produced after the samples irradiation in TRIGA MARK I IPR-R1 research reactor was taken into account. These values were useful to evaluate the radionuclides contamination. The induced activities at the end of an irradiation time t were calculated by the Eq. (1) [24].

$$A_0 = \frac{m \cdot \theta}{A} \cdot N_A \cdot \left[\left(\sigma_\gamma \cdot \Phi_{th}\right) + \left(I_\gamma \cdot \Phi_{epi}\right)\right] \cdot \left(1 - e^{-\lambda \cdot t}\right) \quad (1)$$

in which m is the mass of the irradiated element; θ is the isotope abundance; A is the atomic mass of the isotope; N_A is the Avogadro number; Φ_{th} and Φ_{epi} are the thermal and epithermal neutron flux, respectively; σ_γ is the thermal neutron cross-section of the target nuclei; I_γ is the resonance integral of the target nuclei; λ is the radionuclide decay constant ($\lambda = \ln 2/T_{1/2}$; $T_{1/2}$ is the radionuclide half-life).

The following data were considered in calculations: the elemental composition of the samples determined by INAA; the phosphorus content of 20 % in weight (equal to β-TCP); and 8 h of irradiation time in the central tube position. The central tube has thermal and epithermal neutron flux of 2.8×10^{12} and 2.6×10^{11} n cm^{-2} s^{-1}, respectively.

3 Results and discussion

3.1 X-ray diffractometry (XRD)

Figure 1 shows the XRD patterns of the powders. Several crystalline phases were identified on the patterns: hydroxyapatite (HAp), β-tricalcium phosphate (β-TCP), samarium phosphate ($SmPO_4$), holmium phosphate ($HoPO_4$), dicalcium phosphate (DCP), calcium oxide (CaO). From CaP spectrum, the main phase was HAp with the presence of traces of CaO. From CaP–Ho spectrum, HAp and β-TCP were detected as main phases, and $HoPO_4$ as minor phase. From CaP–Sm spectrum, β-TCP was the main phase and the minor ones were HAp, $SmPO_4$ and DCP. The calcium deficiency could be responsible for β-TCP phase formation in CaP–Sm, and for β-TCP/HAp biphasic formation in CaP–Ho. The calcium deficient apatite calcined above 700 °C could be transformed into β-TCP, as described by Eq. (2) [25].

$$Ca_9(HPO_4)(PO_4)_5(OH) \rightarrow 3Ca_3(PO_4)_2 + H_2O \quad (2)$$

3.2 Fourier transform infrared spectroscopy (FTIR)

Figure 2 illustrates the FTIR transmission spectra of the calcined bioceramics. From CaP spectrum, the bands at 569, 602, 962, 1045 and 1090 cm^{-1} were assigned to internal modes of orthophosphate (PO_4^{3-}) of HAp [26, 27]. The hydroxyl (OH^-) bands at 631 and 3572 cm^{-1} are typical of HAp. The bands at 727, 1157, 1188 and 1211 cm^{-1} were assigned to pyrophosphate ($P_2O_7^{4-}$) modes in calcium pyrophosphate (CPP) [28–30]. The bands at 877 and 1458 cm^{-1} were related to carbonate in substitution of orthophosphate in HAp. This type of group comes from atmospheric carbon dioxide and creates the carbonated hydroxyapatite type B (CHAp) [31, 32]. Thus, it is believed that the calcium oxide observed by XRD resulted from CHAp decomposition during thermal treatment [33].

From CaP–Sm spectrum, the bands at 455, 496, 555, 586, 609, 943, 972, 1030, 1043, 1065 and 1101 cm^{-1} were assigned to internal modes of orthophosphate in β-TCP [33]. The very weak hydroxyl band at 3572 cm^{-1} is attributed to a discrete content of HAp. CPP was identified by the pyrophosphate bands at 727, 1157, 1188 and 1211 cm^{-1}.

The CaP–Ho spectrum showed typical HAp bands. The shifting of orthophosphate bands at 557 and 604 cm^{-1} approaching β-TCP orthophosphate bands at 555 and 609 cm^{-1}, revealed the β-TCP presence. The shading bands

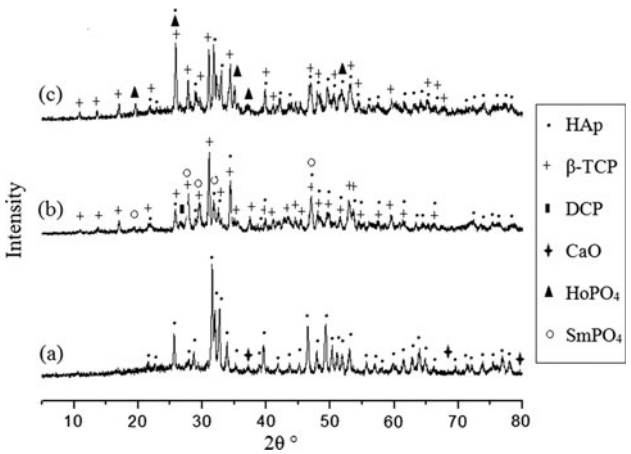

Fig. 1 XRD patterns of calcined powders: CaP (*a*), CaP–Sm (*b*) and CaP–Ho (*c*)

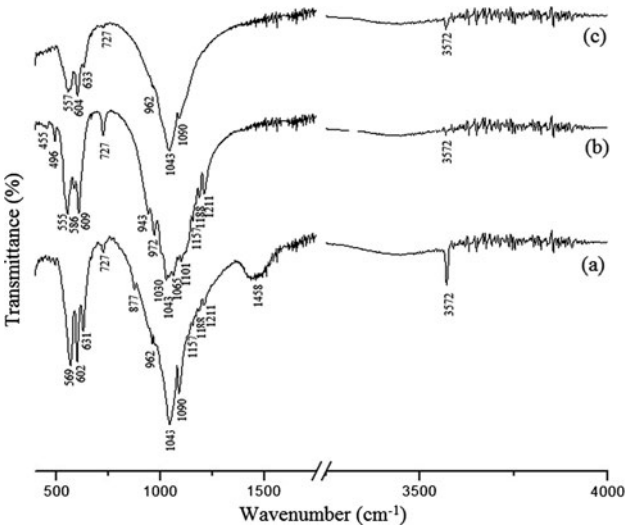

Fig. 2 FTIR spectra of calcined powders: CaP (*a*), CaP–Sm (*b*) and CaP–Ho (*c*)

at 943 and 972 cm^{-1} and the less-intense hydroxyl bands supported this statement. The very weak band at 727 cm^{-1} was associated to a small content of CPP.

The CPP was present in all the bioceramics, since it is a frequent by-product of HA and β-TCP synthesis [34]. CPP is produced after calcination when the synthesis is deficient in calcium. However, this phase was not observed in XRD likely because it was in small quantities. At the same time, other compounds were identified by XRD, but were not identified by FTIR. These inequalities come from the differences of their detection limits. Furthermore, the analysis becomes inaccurate when the sample has a diversified composition. Due to overlaps, the minor compounds can be hidden by the major compounds. Indeed, XRD and FTIR are complementary analytical techniques to identify the composition. The chemical composition of the bioceramics can be summarized as follow: (i) the bioceramic CaP is mainly composed by HAp, and CHAp, CPP and CaO are minor compounds; (ii) the bioceramic CaP–Ho is mainly composed by HAp and β-TCP, and as minor compounds $HoPO_4$ and CPP; and (iii) the bioceramic CaP–Sm is mainly composed by β-TCP, and as minor compounds $SmPO_4$, HAp, CPP and DCP.

When compared to β-TCP, HAp is a more stable phase under physiological conditions, as it has a lower solubility and, thus, slower resorption kinetics. Therefore, due to a higher biodegradability of the β-TCP component, the reactivity of biphasic formulations of HAp with β-TCP increases with the β-TCP/HAp ratio [35, 36]. The CPP and CaO phases are common impurities in commercial bone substitutes [37]. Despite that, CPP is biocompatible and bioactive, as reported previously [38, 39]. Also, the CHAp and DCP are bioactive-resorbable components of bone

Table 1 CaP–Ho and CaP–Sm elemental composition

Bioceramic	Elemental composition (wt%)		
	Ca	Ho	Sm
CaP	38 ± 1	–	–
CaP–Ho	29 ± 1	13.7 ± 0.5	–
CaP–Sm	24 ± 1	–	8.9 ± 0.6

cements and substitutes [37, 40]. Some biodistributions studies lanthanides chelates and materials containing Ho and Sm have been presented in literature [41–43] Indeed, the in vitro performance of Sm_2O_3 as bone substituting material was demonstrated by Herath et al. [44]. However, there are no reports about biological behaviour of $HoPO_4$ and $SmPO_4$ as bone cement material. Although the compound rejection would not be expected, once they are incorporated in a biocompatible matrix, the biological mechanisms in bone need to be investigated [45].

3.3 Instrumental neutron activation analysis (INAA)

The elemental mass concentrations of bioceramics, obtained by INAA, are given in Table 1. The CaP sample showed Ca content of 38 %, near from HAp (Ca = 39.9 %). In fact, they have a reasonable difference considering that CPP (Ca = 31.5 %) was detected on CaP. In both CaP–Ho and CaP–Sm samples, the Ca contents were smaller than in CaP. This result is justified by the presence of phases absent of Ca, e.g., $HoPO_4$ and $SmPO_4$, and phases with less Ca content, as β-TCP (Ca = 38.8 %) and CPP (Ca = 31.5 %).

3.4 Scanning electron microscopy (SEM)

The morphologic aspect of the bioceramics can be observed by SEM, as shown in Fig. 3. It is possible to identify some agglomeration of needle-like HAp nanoparticles with 100–200 nm diameter in Fig. 3b, but it is not clear at CaP–Ho in Fig. 3d, because grains have a denser aspect. Particle's densification, due to calcination process at 700 °C, can be seen in all bioceramics and was depicted in greater magnification at Fig. 3a, c, e. In spite of the dense appearance, spherical nanoparticles with 50 nm diameter, probably β-TCP particles were observed in CaP–Sm in Fig. 3e, f.

3.5 Gamma spectroscopy

The gamma emission spectra of the radioactive CaP–Ho and CaP–Sm powders were presented in Fig. 4. The peaks at 42 and 47 keV are K-edge X-rays from Eu-153, daughter nuclide of Sm-153. The peaks at 49 and 56 keV are K-edge X-rays from Er-166, daughter nuclide of Ho-166. As expected, the gamma emission spectra evidenced Ho-166

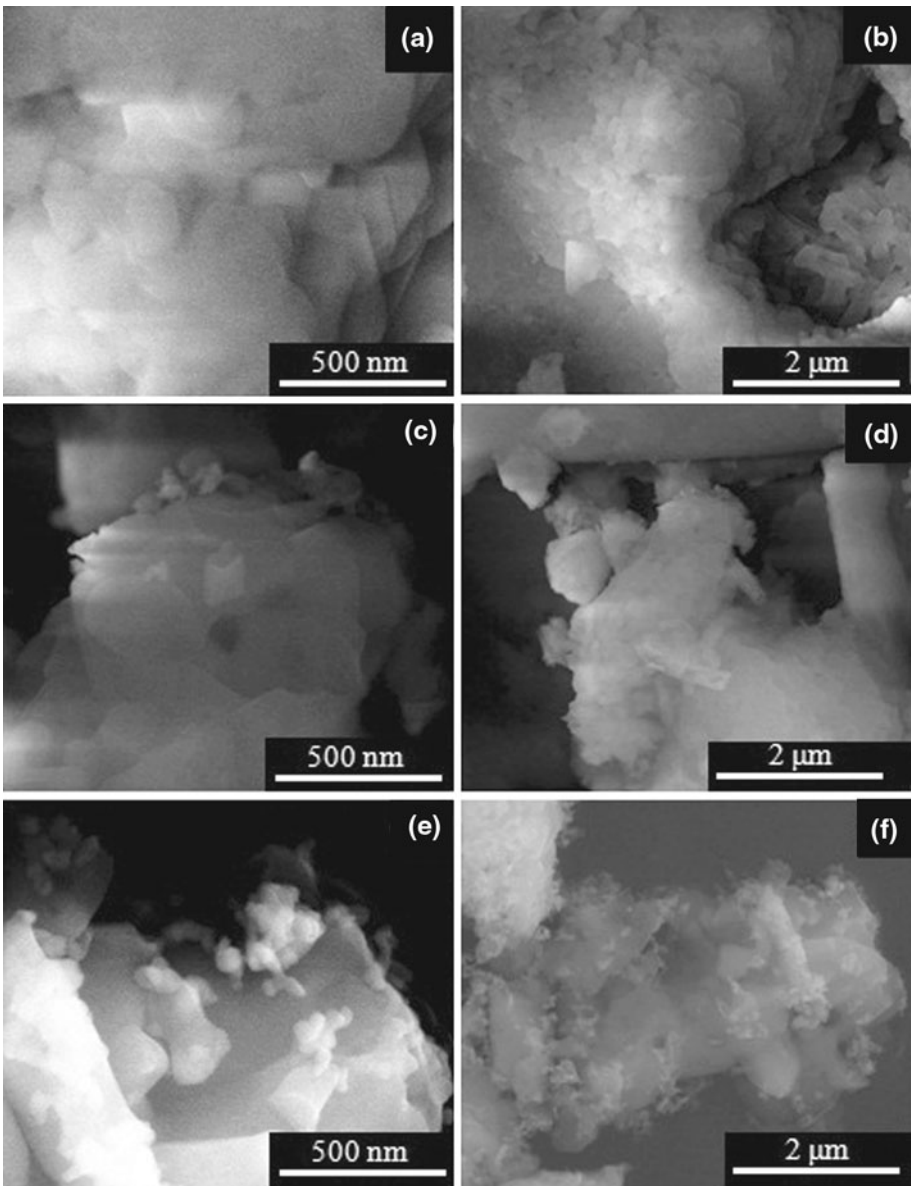

Fig. 3 SEM micrographs of the calcined powders: CaP (**a**, **b**), CaP–Ho (**c**, **d**) and CaP–Sm (**e**, **f**)

and Sm-153 as major radionuclides in radioactive CaP–Ho and CaP–Sm samples, respectively. Even though there were other radionuclides produced after Ca, Sm and P activation, they did not appear by reasons of their very low activities. Specifically the radionuclide P-32, a pure beta-emitter, could not be identified by gamma spectrometry.

3.6 Theoretical estimation of specific activity

Tables 2 and 3 display the theoretical estimation of the specific activities of each radionuclide produced after neutron activation, together with some nuclear data. To evaluate the relevance of radionuclides contaminants, it was assumed as standard the natural activity of 4.4 kBq of K-40 distributed in whole human body [46]. It was determined 01 mg of bioceramic powder content inside the vertebrae, since this amount is enough to reach the therapeutic activity required for the radiovertebroplasty.

After CaP–Ho activation, the specific activity assigned to the radionuclide of interest Ho-166 was 32.5 MBq mg^{-1}, as given in Table 2. The radionuclides Ca-41, Ca-45 and Ca-47 achieved activities lower than K-40, so they can be neglected. The radionuclide Ca-49 had initial activity higher than K-40, but it decays quickly with half-life of 8.72 min. The radionuclide P-32 had initial activity of 32.8 kBq, since it is a pure beta-emitter with half-life of 14.28 days; therefore, P-32 can contribute together with Ho-166 to absorbed doses nearby the bone cement.

After CaP–Sm activation, the specific activity assigned to the radionuclide of interest Sm-153 was 14.5 MBq mg^{-1}, as shown in Table 3. The Ca-41, Ca-45, Ca-47 and Sm-145 radionuclides reached activities lower than K-40, then such

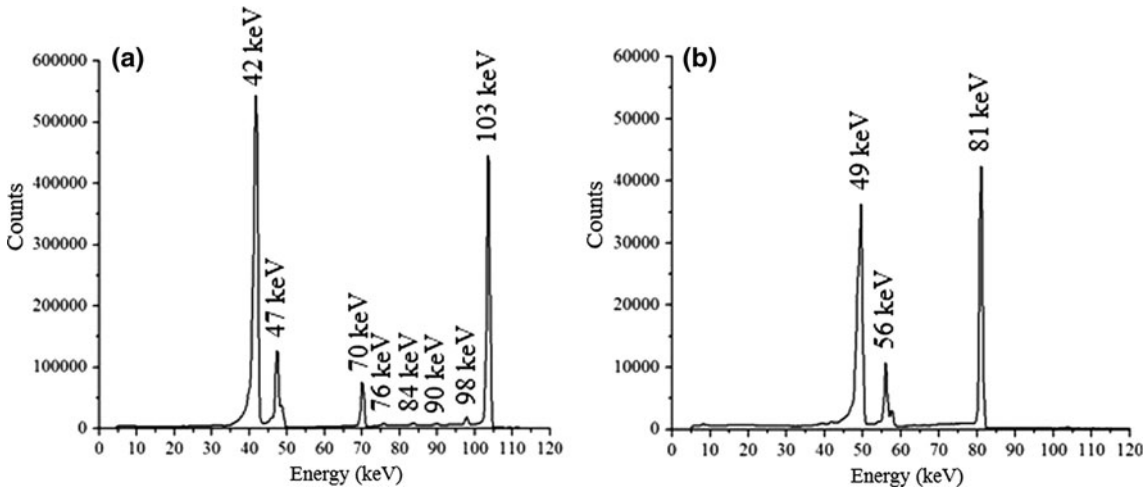

Fig. 4 Gamma emission spectrum of CaP–Sm (**a**) and CaP–Ho (**b**)

Table 2 Theoretical estimation of induced activities assigned to each radionuclide produced after CaP–Ho neutron activation

Nuclide	Concentration (wt%)	Natural abundance (%)	σ_γ (barn)	I_γ (barn)	Radionuclide	Half-life	Specific activity (kBq/mg)
P-31	20	100	0.18	0.08	P-32	14.28 days	3.28×10^{1}
Ca-40	29	96.941	0.41	0.22	Ca-41	103,000 years	3.14×10^{-5}
Ca-44		2.086	0.84	0.59	Ca-45	162.7 days	2.95×10^{-1}
Ca-46		0.004	0.7	0.9	Ca-47	4.536 days	1.66×10^{-2}
Ca-48		0.187	1.1	0.9	Ca-49	8.72 min	2.26×10^{1}
Ho-165	13.7	100	61	680	Ho-166	1.117 days	3.25×10^{4}

Table 3 Theoretical estimation of induced activities assigned to each radionuclide produced after CaP–Sm neutron activation

Nuclide	Concentration wt%	Natural abundance %	σ_γ (barn)	I_γ (barn)	Radionuclide	Half-life	Specific activity (kBq/mg)
P-31	20	100	0.18	0.08	P-32	14.28 days	3.28×10^{1}
Ca-40	24	96.941	0.41	0.22	Ca-41	103,000 years	2.60×10^{-5}
Ca-44		2.086	0.84	0.59	Ca-45	162.7 days	2.44×10^{-1}
Ca-46		0.004	0.7	0.9	Ca-47	4.536 days	1.37×10^{-2}
Ca-48		0.187	1.1	0.9	Ca-49	8.72 min	1.87×10^{1}
Sm-144	8.9	3.07	1.6	2.4	Sm-145	340 days	3.97×10^{-2}
Sm-152		26.75	208	3,000	Sm-153	1.929 days	1.45×10^{4}
Sm-154		22.75	7	40	Sm-155	22.2 min	2.38×10^{3}

activities can also be neglected. The radionuclides Ca-49 and Sm-155 exhibited initial activities higher than K-40, but decay quickly with half-life of few minutes. For the same past reasons, the pure beta-emitter P-32 can contribute along with Sm-153 to absorbed doses nearby the bone cement.

It is worth mentioning that these specific activities are as high as the irradiation time is longer. Thus the specific activities can be decreased or increased, satisfying the treatment requirements.

4 Conclusions

Bioceramics powders of calcium phosphate incorporated with Ho and Sm can be synthesized by sol–gel route using

simple processing and reagents. The powders were identified as multiphasic calcium phosphates with the presence of holmium phosphate and samarium phosphate. Ho-166 and Sm-153 were the main radioisotopes produced after the neutron activation, with activities estimated at MBq per milligram of bioceramic powder. These radioactive bioceramics constitute promising biomaterials for radiovertebroplasty, a novel therapy modality for spine tumors. However, their bioactivity as well as their efficacy on spine tumors treatment must be investigated in clinical trials.

Acknowledgments The authors would like to thank Conselho Nacional de Desenvolvimento Científico (CNPq) e Tecnológico for grant support, Centro de Desenvolvimento da Tecnologia Nuclear (CDTN/CNEN), Departamento de Química da Universidade Federal de Minas Gerais (DQ-UFMG) and Centro de Microscopia da UFMG, for experimental support.

References

1. Wong DA, Fornasier VL, MacNab I. Spinal metastases: the obvious, the occult, and the imposters. Spine. 1990;15:1–4.
2. Gerszten PC, Germanwala A, Burton SA, Welch WC, Ozhasoglu C, Vogel WJ. Combination kyphoplasty and spinal radiosurgery: a new treatment paradigm for pathological fractures. J Neurosurg Spine. 2005;3:296–301.
3. Kaneko TS, Sehgal V, Skinner HB, Al-Ghazi MSAL, Ramisinghani NS, Keyak JH. Evaluation of a radiation transport modeling method for radioactive bone cement. Phys Med Biol. 2010;55:2451–63.
4. Bilsky MH, Lis E, Raizer J, Lee H, Boland P. The diagnosis and treatment of metastatic spinal tumor. Oncologist. 1999;4:459–69.
5. Kuo JV, Cabebe E, Al-Ghazi M, Yakoob I, Ramsinghani NS, Sanford R. Intensity-modulated radiation therapy for the spine at the University of California, Irvine. Med Dosim. 2002;27:137–45.
6. Haley ML, Gerszten PC, Heron DE, Chang YF, Atteberry DS, Burton SA. Efficacy and cost-effectiveness analysis of external beam and stereotactic body radiation therapy in the treatment of spine metastases: a matched-pair analysis. J Neurosurg Spine. 2011;14:537–42.
7. Helissey C, Levy A, Jacob J, Dutertre G, Tardo-Dino PE, Bauduceau O, Vedrine L, Chargari C. External beam radiotherapy in the management of spinal metastases: review of current strategies and perspectives for highly conformal irradiation modalities. Discov Med. 2011;11:505–11.
8. Macedo RD, Campos TPR. Radiovertebroplastia para tratamento de neoplasias malignas ósseas da coluna vertebral. Internacional Nuclear Atlantic Conference INAC 2005, Santos 2005. p. 1–5.
9. Campos TPR, Macedo RD. Compósito Ósseo Radioativo, Patent PI0605721-7 A2, 2006.
10. Hirsch AE, Medich DC, Rosenstein BS, Martel CB, Hirsch JA. Radioisotopes and vertebral augmentation: dosimetric analysis of a novel approach for the treatment of malignant compression fractures. Radiother Oncol. 2008;87:119–26.
11. Silveira MC, Campos TPR. Avaliação radiodosimétrica através do código MCNP-5 da radiosteoplastia em tumores ósseos nos membros. Matéria. 2007;12:186–92.
12. Ashamalla H, Cardoso ER, Macedon M, Guirguis A, Weng L, Ali S, Mokhtar B, Ashmalla M, Panigrahi N. Phase I trial of vertebral intracavitary cement and samarium (VICS): novel technique for treatment of painful vertebral metastasis. Int J Radiat Oncol Biol Phys. 2009;75:836–42.
13. Cardoso ER, Ashamalla H, Weng L, Mokhtar B, Ali S, Macedon M, Guirguis A. Percutaneous tumor curettage and interstitial delivery of samarium-153 coupled with kyphoplasty for treatment of vertebral metastases. J Neurosurg Spine. 2009;10:336–42.
14. Lu J, Deng J, Zhao H, Shi M, Wang J, Zhao L. Safety and feasibility of percutaneous vertebroplasty with radioactive 153Sm PMMA in an animal model. Eur J Radiol. 2011;78:296–301.
15. Jasper LE, Deramond H, Mathis JM, Belkoff SM. Material properties of various cements for use in vertebroplasty. J Mat Sci Mat Med. 2002;13:1–5.
16. Heini PF, Berlemann U. Bone substitutes in vertebroplasty. Eur Spine J. 2001;10:205–13.
17. Lieberman IH, Togawa D, Kayanja MM. Vertebroplasty and kyphoplasty: filler materials. Spine J. 2005;5:305–16.
18. Hernández L, Gurruchaga M, Goñi I. Injectable acrylic bone cements for vertebroplasty based on a radiopaque hydroxyapatite: formulation and rheological behavior. J Mater Sci Mater Med. 2009;20:89–97.
19. Komath M, Varma HK. Development of a fully injectable calcium phosphate cement for orthopedic and dental applications. Bull Mater Sci. 2003;26:415–22.
20. Webster TJ, Massa-Schlueter EA, Smith JL, Slamovich EB. Osteoblast response to hydroxyapatite doped with divalent and trivalent cations. Biomaterials. 2004;25:2111–21.
21. Chow LC. Next generation calcium phosphate-based biomaterials. Dent Mater J. 2009;28:1–10.
22. Dorozhkin SV. Bioceramics of calcium orthophosphates. Biomaterials. 2010;31:1465–85.
23. Menezes MABC, Palmieri HEL, Leonel LV, Nalini HA, Jaćimović R. Iron Quadrangle, Brazil: elemental concentration determined by k0-instrumental neutron activation analysis. Part I: soil samples. J Radioanal Nucl Chem. 2006;270:111–6.
24. Parry SJ. Handbook of neutron activation analysis. 1st ed. Surrey: Viridian Publishing; 2003.
25. Sz-Chian L, San-Yuan C. Transformation mechanism of different chemically precipitated apatitic precursors into b-tricalcium phosphate upon calcinations. Biomaterials. 2002;23:4541–7.
26. Peña J, Vallet-Regí M. Hydroxyapatite, tricalcium phosphate and biphasic materials prepared by a liquid mix technique. J Eur Ceram Soc. 2003;23:1687–96.
27. Fowler BO. Infrared studies of apatites, vibrational assignments for calcium, strontium and barium hydroxyapatites utilizing isotopic substitution. Inorg Chem. 1974;13:194–207.
28. El Kady AM, Mohamed KR, El-Bassyouni GT. Fabrication, characterization and bioactivity evaluation of calcium pyrophosphate/polymeric biocomposites. Ceram Int. 2009;35:2933–42.
29. Loher S, Stark WJ, Maciejewski M, Baiker A, Pratsinis SE, Reichardt D, Maspero F, Krumeich F, Günther D. Fluoro-apatite and calcium phosphate nanoparticles by flame synthesis. Chem Mater. 2005;17:36–42.
30. Hezel A, Ross SD. The far infra-red spectra of some divalent metal pyrophosphates. Spectrochim Acta A. 1968;24:131–5.
31. Chen J, Wang Y, Chen X, Ren L, Lai C, He C, Zhang Q. A simple sol-gel technique for synthesis of nanostructured hydroxyapatite, tricalcium phosphate and biphasic powders. Mater Lett. 2011;65:1923–6.
32. Layrolle P, Ito A, Tateishi T. Sol-gel synthesis of amorphous calcium phosphate and sintering into microporous hydroxyapatite bioceramics. J Am Ceram Soc. 1998;81:1421–8.
33. Suchanek WL, Shuk P, Byrappa K, Riman RE, TenHuisenb KS, Janas VF. Mechanochemical–hydrothermal synthesis of carbonated apatite powders at room temperature. Biomaterials. 2002;23:699–710.
34. Jillavenkatesa A, Condrate RA. The infrared and Raman spectra of β-and α-tricalcium phosphate. Spectrosc Lett. 1998;31:1619–34.

35. Destainville A, Champion E, Bernache-Assollant D, Laborde E. Synthesis, characterization and thermal behavior of apatitic tricalcium phosphate. Mater Chem Phys. 2003;80:269–77.
36. Dorozhkin SV. Biphasic, triphasic and multiphasic calcium orthophosphates. Acta Biomater. 2012;8:963–77.
37. Tadic D, Epple M. A thorough physicochemical characterisation of 14 calcium phosphate-based bone substitution materials in comparison to natural bone. Biomaterials. 2004;25:987–94.
38. Kitsugi T, Yamamuro T, Nakamura T, Oka M. Transmission electron microscopy observations the interface of bone and four types of calcium phosphate ceramics with different calcium/phosphorus molar ratios. Biomaterials. 1995;16:1101–7.
39. Lee JH, Lee DH, Ryu HS, Chang B, Hong KS, Lee CK. Porous beta-calcium pyrophosphate as a bone graft substitute in a canine bone defect model. Key Eng Mat. 2003;240–42:399–402.
40. Liu C, Gai W, Pan S, Liu Z. The exothermal behavior in the hydration process of calcium phosphate cement. Biomaterials. 2003;24:2995–3003.
41. Neves M, Teixeira FC, Antunes I, Majkowska A, Gano L, Santos AC. Chemical and biological evaluation of (153)Sm and (46/47)Sc complexes of indazolebisphosphonates for targeted radiotherapy. Appl Radiat Isot. 2011;69:80–4.
42. Unnia PR, Chaudharib PR, Venkatesha M, Ramamoorthya N, Pillaia MRA. Preparation and bioevaluation of 166Ho labelled hydroxyapatite (HA) particles for radiosynovectomy. Nucl Med Biol. 2002;29:199–209.
43. Das T, Chakraborty S, Sarma HD, Venkatesh M, Banerjee S. 166Ho-labeled hydroxyapatite particles: a possible agent for liver cancer therapy. Cancer Biother Radiopharm. 2009;29:7–13.
44. Herath HMTU, Di Silvio L, Evans JRG. In vitro evaluation of samarium (III) oxide as a bone substituting material. J Biomed Mater Res A. 2010;94:130–6.
45. Vidaud C, Bourgeois D, Meyer D. Bone as target organ for metals: the case of f-elements. Chem Res Toxicol. 2012;25:1161–75.
46. ICRP. Limits for intakes of radionuclides by workers. ICRP Publication 30 (Part 1). Ann. ICRP 2 1979. 3–4.